# Supporting Information

**Ultrahigh-temperature Film Capacitors via Homo/Heterogeneous Interfaces**

Rui Lu, ‡[ab] Zhonghui Shen, ‡[cd] Chunrui Ma, ‡[*b], Tingzhi Duan,[ab] Lu Lu,[ab] Guangliang Hu,[ab] Tian-Yi Hu, [b] Caiyin You,[e] Shaobo Mi,[*b] Chun-Lin Jia,[ab] Long-Qing Chen,[*f] and Ming Liu[*ab]

[a] School of Microelectronics, Xi'an Jiaotong University, Xi'an, China.

[b] State Key Laboratory for Mechanical Behavior of Materials, Xi'an Jiaotong University, Xi'an, China.

[c] State Key Laboratory of Advanced Technology for Materials Synthesis and Processing, Center of Smart Materials and Devices, Wuhan University of Technology, Wuhan, China.

[d] International School of Materials Science and Engineering, Wuhan University of Technology, Wuhan, China.

[e] School of Materials Science and Engineering, Xi'an University of Technology, Xi'an, China.

[f] Department of Materials Science and Engineering, The Pennsylvania State University, University Park, Pennsylvania, United States.

‡These authors contributed equally to this work.

*Corresponding author. Email:

chunrui.ma@xjtu.edu.cn (C. Ma), shaobo.mi@xjtu.edu.cn (S.-B. Mi),

lqc3@psu.edu (L.-Q. Chen), m.liu@xjtu.edu.cn (M. Liu).

**Simulation Methods**

**Phase-field Simulations**

In this work, we design four representative dielectrics to study the interface effect on energy storage: pure matrix (PM), vertical interface (VI), parallel interface (PI) and interlayer interface (II), as shown in Figure. 1a-1d.

For the thermal transport simulation, the heat transport process is described by

$$\rho(\mathbf{r})c_p(\mathbf{r})\frac{\partial T(\mathbf{r},t)}{\partial t} = \kappa(\mathbf{r})\nabla T^2(\mathbf{r},t) + \sigma(\mathbf{r},T)E^2 \tag{S1}$$

where $\rho$, $c_p$, $\kappa$ and $\sigma$ are the density, constant-pressure heat capacity, thermal conductivity and electrical conductivity, respectively. The applied electric field is fixed at 100 MV/m, and the heat flux at boundaries is assumed to be controlled by the convective heat transfer by

$$n(-\kappa\nabla T) = h(T - T_{\text{sur}}) \tag{S2}$$

where $T_{\text{sur}}$ is the surrounding temperature with a value of 293K and $h$ is the convective heat transfer coefficient with a value of 10 W/m$^{-2}$ K$^{-1}$. To reflect the differences of matrix and interface phase on electrical and thermal properties, the electrical conductivities are set with 1e$^{-8}$ S m$^{-1}$ for matrix and 1e$^{-10}$ S m$^{-1}$ for interface phase, and the thermal conductivities are considered as 12 W m$^{-1}$ K$^{-1}$ for interface phase and 7 W m$^{-1}$ K$^{-1}$ for matrix

Inspired by the damage evolution in composites[1], we build a phase-field model to simulate the breakdwon process in dielectrics. Here, we introduce an order parameter $\eta(\mathbf{r},t)$ to describe the dielectric response under different electric fields, including polarization and breakdown process. $\eta(\mathbf{r},t)$=1 represents the breakdown phase, $\eta(\mathbf{r},t)$=0

2

represents the non-breakdown phase. Here, the free energy in inhomogeneous system includes the phase separation $f_{\text{sep}}$, the gradient energy $f_{\text{grad}}$ and electrostatic energy density $f_{\text{elec}}$ as follows:

$$F = \int_V \left[ f_{\text{sep}}\left(\eta(\mathbf{r})\right) + f_{\text{grad}}\left(\eta(\mathbf{r})\right) + f_{\text{elec}}\left(\eta(\mathbf{r})\right) \right] dV \tag{S3}$$

Here, to describe the phase transtion between broken phase and unbroken phase, the phase separation energy is defined by a double-well function,

$$f_{\text{sep}}\left(\eta(\mathbf{r})\right) = \alpha \eta^2 \left(1 - \eta\right)^2 \tag{S4}$$

where $\alpha$ is a positive coefficient describing the energy barrier of the phase separation with a value of $10^8$ J/m$^3$ in this work. The gradient energy is expressed as

$$f_{\text{grad}}\left(\eta(\mathbf{r})\right) = \frac{1}{2} \gamma \left| \nabla \eta(\mathbf{r}) \right|^2 \tag{S5}$$

where $\gamma$ is the gradient energy coefficient with the value of $10^{-10}$ J/m. The electrostatic energy can be calculated by

$$f_{\text{elec}}\left(\eta(\mathbf{r})\right) = -\frac{1}{2} \varepsilon_0 \varepsilon_{ij}(\mathbf{r}) E_i(\mathbf{r}) E_j(\mathbf{r}) \tag{S6}$$

where $\varepsilon_{ij}(\mathbf{r})$ is the spatially dependent permittivity, $E_i(\mathbf{r})$ is the total electric field component. In order to describe the matrix and the nanofillers in the nanocomposite, a non-evolving field variable $\rho(\mathbf{r})$ is introduced, which takes the value of 1 in the interface phase and 0 in the matrix. Then, the spatially dependent permittivity could be written as:

$$\varepsilon_{ij}(\mathbf{r}) = \eta^3 \left(10 - 15\eta + 6\eta^2\right) \varepsilon_{ij}^{\text{B}} + \left[1 - \eta^3 \left(10 - 15\eta + 6\eta^2\right)\right] \times$$
$$\left\{ \rho^3 \left(10 - 15\rho + 6\rho^2\right) \varepsilon_{ij}^{\text{I}} + \left[1 - \rho^3 \left(10 - 15\rho + 6\rho^2\right)\right] \varepsilon_{ij}^{\text{M}} \right\} \tag{S7}$$

where $\varepsilon_{ij}^{\text{B}}$, $\varepsilon_{ij}^{\text{I}}$, and $\varepsilon_{ij}^{\text{M}}$ indicate the permittivity of the breakdown phase, interface phase, and the matrix, respectively.

3

A modified Allen-Cahn equation is developed to govern the dynamic process of dielectric breakdown,

$$\frac{\partial \eta(\mathbf{r},t)}{\partial t} = -L_0 H\left(\left|f_{\text{elec}}\right| - \left|f_{\text{critical}}\right|\right)\left[\frac{\partial f_{\text{sep}}(\eta)}{\partial \eta(\mathbf{r},t)} - \gamma\nabla^2\eta(\mathbf{r},t) + \frac{\partial f_{\text{elec}}(\mathbf{r})}{\partial \eta(\mathbf{r},t)}\right] \quad \text{(S8)}$$

where $L_0$ is the kinetic coefficient determining the interface mobility, $H(\left|f_{\text{elec}}\right| - \left|f_{\text{critical}}\right|)$ is the Heaviside unit step function ($H(\left|f_{\text{elec}}\right| < \left|f_{\text{critical}}\right|) = 0$ and $H(\left|f_{\text{elec}}\right| > \left|f_{\text{critical}}\right|) = 1$), and $f_{\text{critical}}$ is the maximal energy density calculated by $f_{\text{critical}} = \frac{1}{2}\varepsilon_0\varepsilon_r E_b^2$. The purpose of introducing the Heaviside function into the Allen-Cahn equation is to assure that the breakdown phase can grow only if the electric energy of a local point is greater than its maximal energy endurance. Thus, one advantage of this model is that we could find the critical breakdown strength of different composites, compared to the fractal dimension breakdown model [2]. The local electric field distribution could be calculated by solving Poisson's equation using the spectral iterative perturbation method as follows:

$$\nabla D = \nabla\left(\varepsilon_0\varepsilon_r E(\mathbf{r})\right) = 0 \quad \text{(S9)}$$

Here, the characteristic length scale $d_0 = \sqrt{\gamma/\alpha}$, and the characteristic time scale $t_0 = 1/(L_0\alpha)$ can be defined in terms of the material parameters $\gamma$, $\alpha$ and $L_0$. A grid size of $N_x\Delta x \times N_y\Delta x \times N_z\Delta x$ with grid space of $\Delta x = d_0$ is employed with $N_x = N_y = 512$ and $N_z = 1$. A time interval $\Delta t = 0.05 t_0$ is used to numerically evolve the kinetic equation. The coefficient $\alpha$ in the separation energy term is given a value of $10^8$ J/m$^3$ to represent the barrier of the breakdown phase and the non-breakdown phase. A value of $10^{-10}$ J/m is used for the gradient energy coefficient $\gamma$ to specify $d_0$ 1nm in the modeling. To reflect the ferroelectric difference between the grain phase and interface phase (grain

boundary), the permittivities of grain phase and interface phase are set with 30 and 100.

Then, their intrinsic breakdown strength is calculated by a thermochemical model [3].

**Target and film fabrication**

A series of stoichiometric $BaHf_xTi_{1-x}O_3$(BHTO) ceramic targets ($x = 0.17, 0.25$ and

0.32) were fabricated by the conventional solid-state sintering methods.[4] High-purity

$BaCO_3$, $TiO_2$ and $HfO_2$ (purity 99.99%) powders were mixed at designed

stoichiometric ratios, ball-milled for 4 h and then calcined at 850°C for 4 h. To

minimize particle size, the calcined powder was further ball-milled. The dry powder

was bindered with an alcohol solution before being crushed into 50 mm diameter

particles at 15 MPa for 15 minutes. The pellets were sintered in a sealed alumina

crucible at 1050°C for 2 hours after the binder was burnt away at 650°C for 2 hours.

## Supplementary Text

### Analying the leakage mechanisms in the BHTO films

Five leakage mechanisms fall into two categories,bulk-limited and interface-limited[5-6]. Ohmic conduction, space charge limited conduction (SCLC) and Poole-Frenkel (P-F) emission are the bulk-limited mechanisms.[7]

$$\text{Ohmic:} \qquad J = en\mu E \text{ ,} \qquad\qquad\qquad (S10)$$

$$\text{SCLC:} \qquad J = \frac{9\mu\varepsilon_0\varepsilon_r}{8} \cdot \frac{E^2}{d} \text{ ,} \qquad\qquad\qquad (S11)$$

$$\text{P-F emission:} \qquad J = e\mu N_c E \cdot \exp\left[ -\frac{\Phi_{PF}}{k_B T} + \frac{1}{k_B T}\left( \frac{e^3 E}{\pi\varepsilon_0 K} \right)^{1/2} \right] \text{,} \qquad (S12)$$

$$\text{Schottky emission:} \qquad J = AT^2 \cdot \exp\left[ -\frac{\Phi_{Schottky}}{k_B T} + \frac{1}{k_B T}\left( \frac{e^3 E}{4\pi\varepsilon_0 K} \right)^{1/2} \right] \text{,} \qquad (S13)$$

$$\text{F-N tunnelling:} \qquad J = \frac{e^2 E^2}{8\pi h\phi_B} \cdot \exp\left[ \frac{-8\pi\left(2em_T^*\right)^{1/2}}{3hE}\phi_B^{3/2} \right] \text{,} \qquad (S14)$$

Where $e, n, \mu, \varepsilon_0, \varepsilon_r, d, N_c, \Phi_{PF}, k_B, T, K, A, \Phi_{schottky}, h, \phi_B, m_T^*$ are electronic charge, electron density,electronic drift mobility, vaccum permittivity, relative permittivity, film thickness,effective density of states of the conduction band, P-F emission energy barrier, Boltzmann constant, absolute temperature, optical permittivity, Richardson constant, Schottky energy barrier, Plank constant, potential barrier height, and effective electron mass, respectively.[7] The $K$ equals the square of the optical refractive index $n$ .[7] The $n$ of HfO$_2$ and BaTiO$_3$ are around 1.98 [7] and 2.49 [8], respectively, Hence BHTO films should have a K value of 3 ~ 7. By fitting to the Ohmic and SCLC leakage mechanisms(shown in Figure S6(a)), we conclude that the ohmic conduction mechanism dominates at low fields (E < E1), At $E > E_{TEL}$(called the trap-filled limit

electric field), the leakage current increases sharply with slope >>2. Through increasing

the interface of the films, we can significantly increase the $E_1$ and $E_{TEL}$ and accordingly

improve the leakage and breakdown properties of the BHTO thin films. Fitting results

exclude the P-F tunneling mechanism at high electric fields, since the $K_{PF}$ values

calculated from slopes of ln ($J/E$) vs $E^{1/2}$ plots are larger than 7 (Figure S6b). Fittings

with F-N and Schottky emissions (Figure S6c and 6d), it is found that F-N and Schottky

emission coexists at high electric filed, but the F-N tunneling plays a dominant role in

all the designed multilayer strucutres.
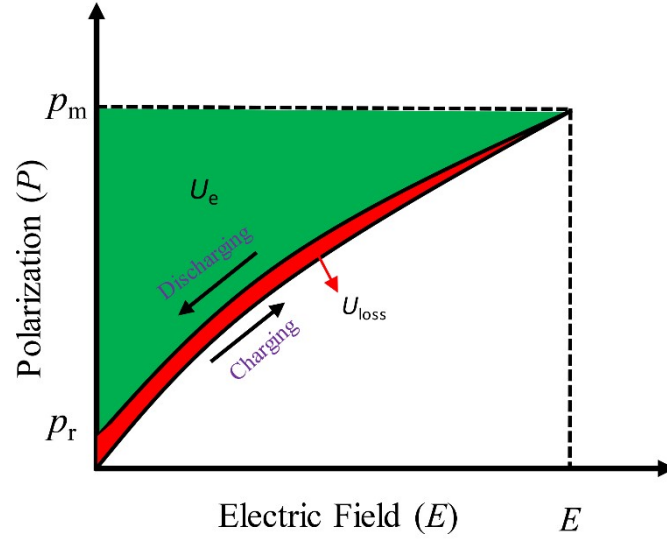
**Figure S1.** Diagrammatic illustration of the energy storage characteristics of the ferroelectric capacitor.

$$U_e = \int_{P_r}^{P_{max}} EdP \tag{S15}$$

where $P_m$ is the maximum polarization and $P_r$ is the remnant polarization. The energy efficiency $\eta$ is expressed as

$$\eta = \frac{U_e}{U_{st}} = \frac{U_e}{U_e + U_{loss}} \times 100\% \tag{S16}$$

The red area represents the energy loss $U_{loss}$ in the charging-discharging cycle due to hysteretic polarization switching and conduction loss. $E_b$ is the breakdown strength, that is a dielectric can sustain the highest electric field.
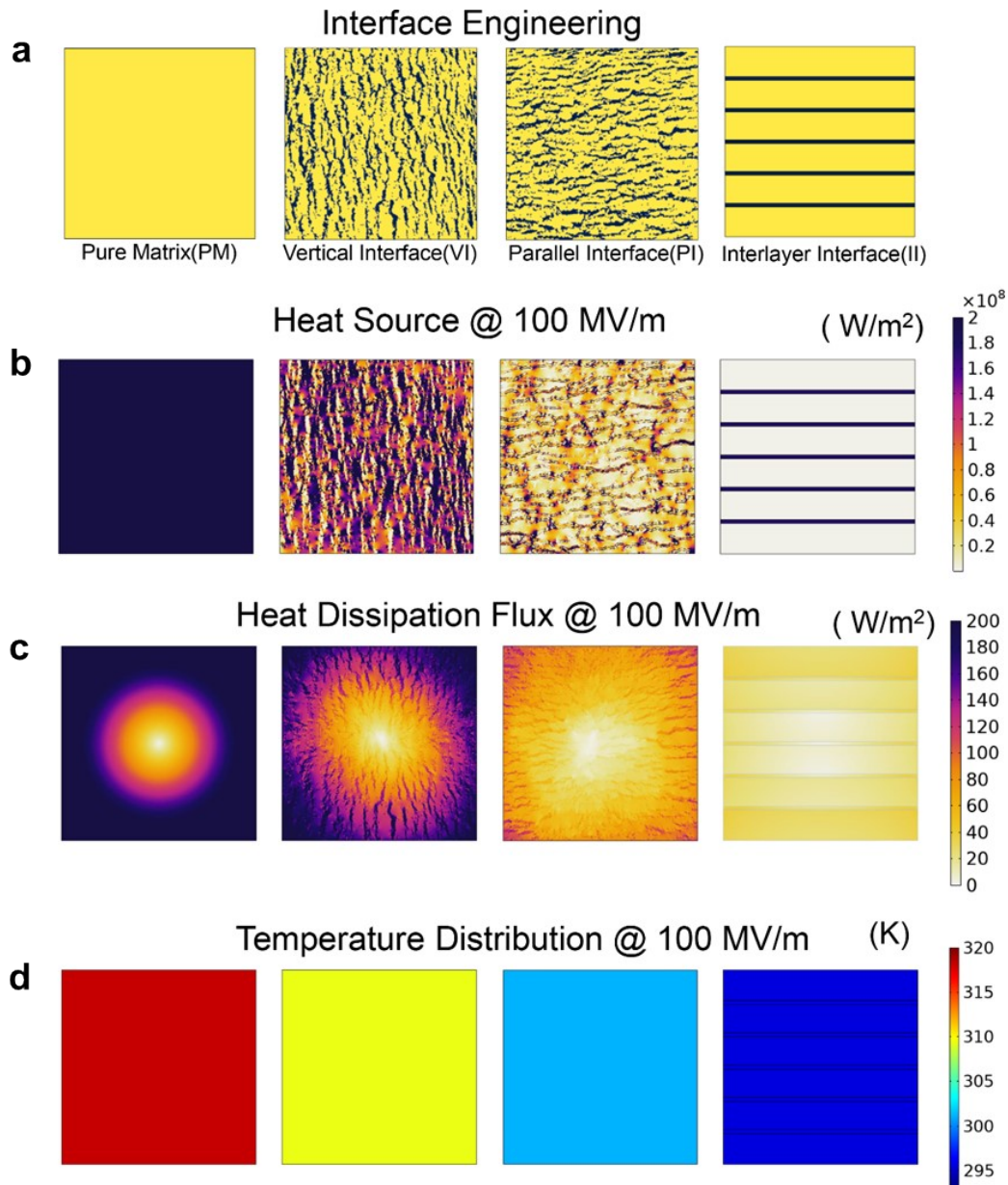
**Figure S2.** The simulated thermal transport process. (a) Schematics of the microstructure in phase-field models based on different interface systems: pure matrix (PM), homogeneous vertical interfaces (VI), homogeneous parallel interfaces (PI) and heterogeneous interlayer interfaces (II), (b) Heat source and corresponding maximal temperature when operating at 100 MV/m, (c) Heat dissipation flux, (d) Temperature distribution.
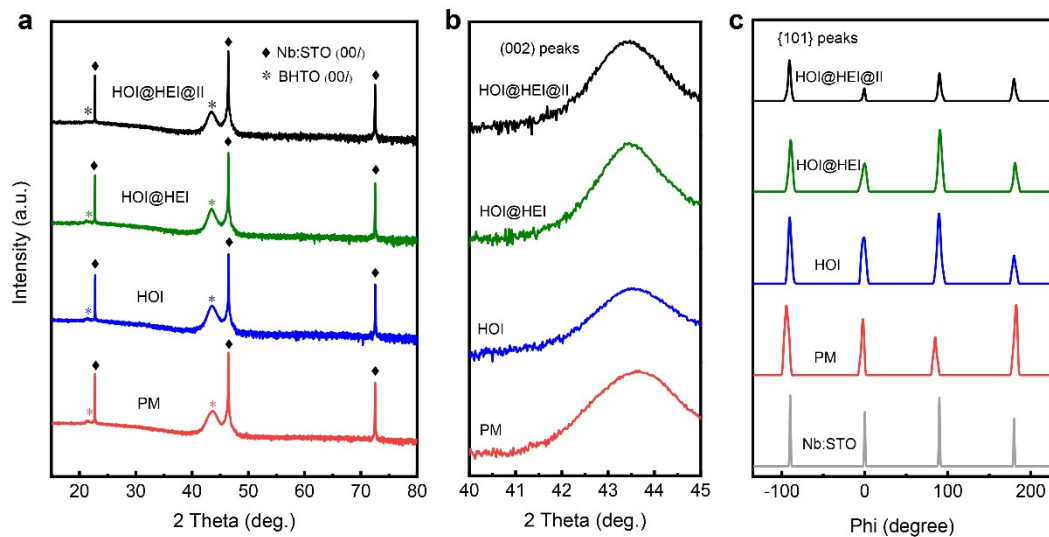
**Figure S3.** XRD patterns of the BHTO films. (a) Theta-2theta, (b) Enlarged $\theta$-$2\theta$ scans near the (002) peak. and (c) phi scans of the BHTO films. All the films are pure perovskites with highly (00$l$) orientations inherited from the substrates. Phi scans further demonstrate the fourth-fold symmetry of the films with a cubic-on-cubic single-crystalline epitaxy.
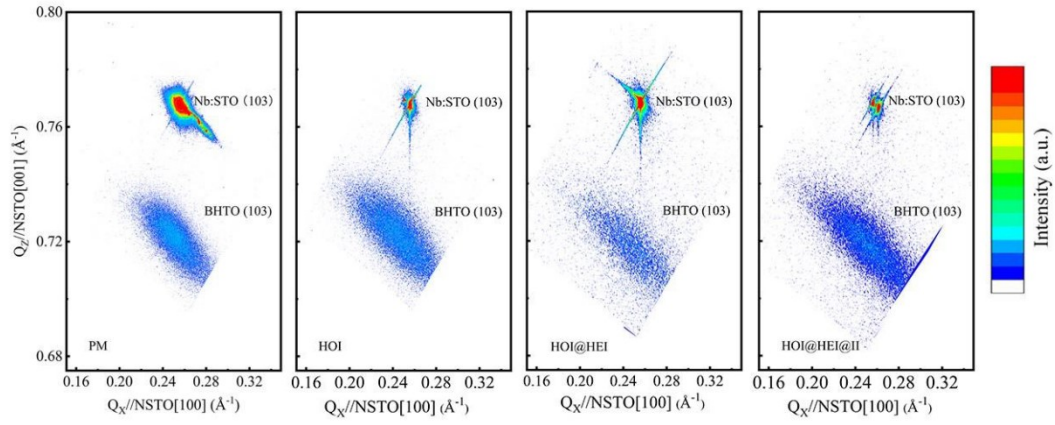
**Figure S4.** Reciprocal space maps results for PM, HOI, HOI@HEI and HOI@HEI@II films around the Nb:STO (103) diffraction spots. Increasing the interface, the spots on the films are gradually stretched.
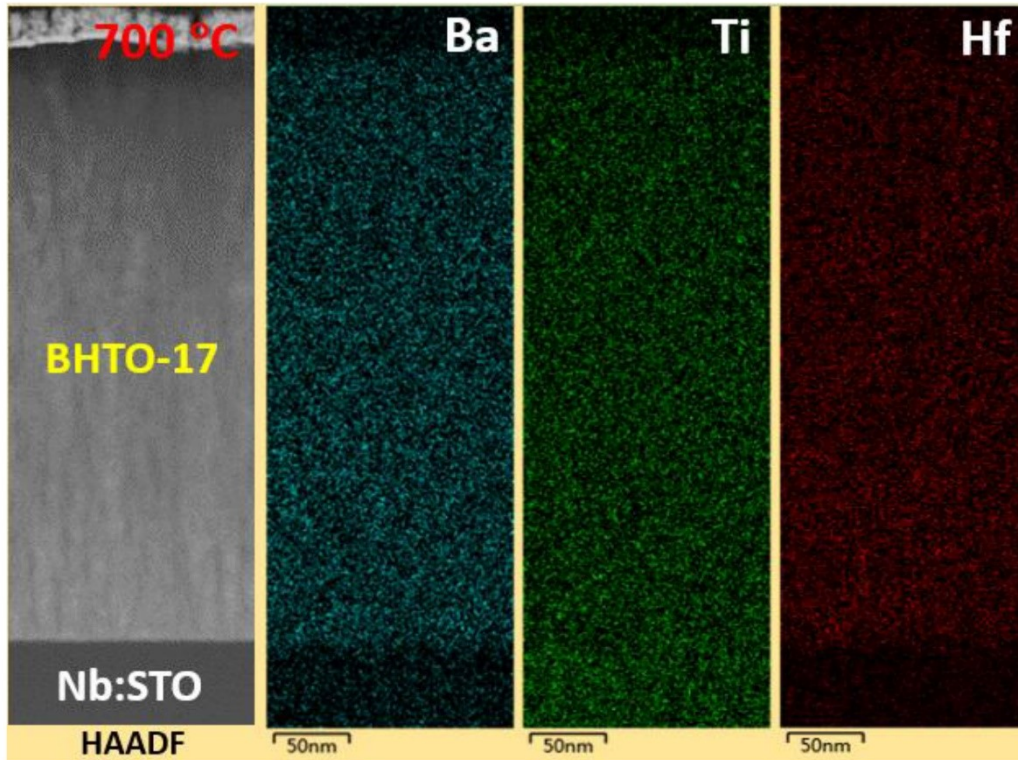
**Figure S5.** No apparent elemental segregation in the BHTO-17 films by energy-dispersive X-ray spectroscopy (EDS) mapping. A HAADF-STEM image of BHTO-17 films prepared on Nb-doped $SrTiO_3$ (001) (Nb:STO) substrates at 700°C, and the corresponding elemental maps of Ba, Ti and Hf, which indicate no apparent elemental segregation within the BHTO-17 films. The HAADF-STEM image was recorded along the [010] direction of the Nb:STO substrate.
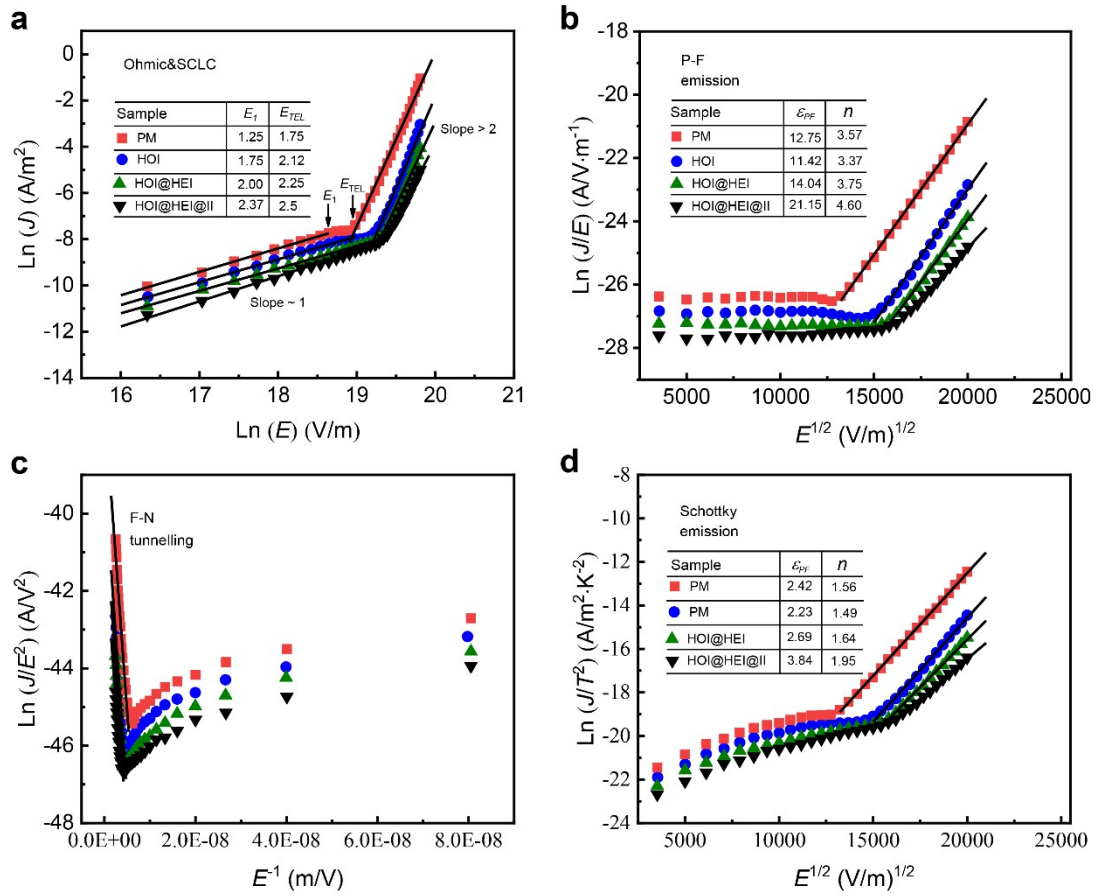
**Figure S6.** Fittings of the leakage current densities of the BHTO films with various conduction mechanisms. (a) Ohmic conduction and space charge limited conduction (SCLC), (b) P-F emission, (c) F-N tunnelling and (d) Schottky emission.
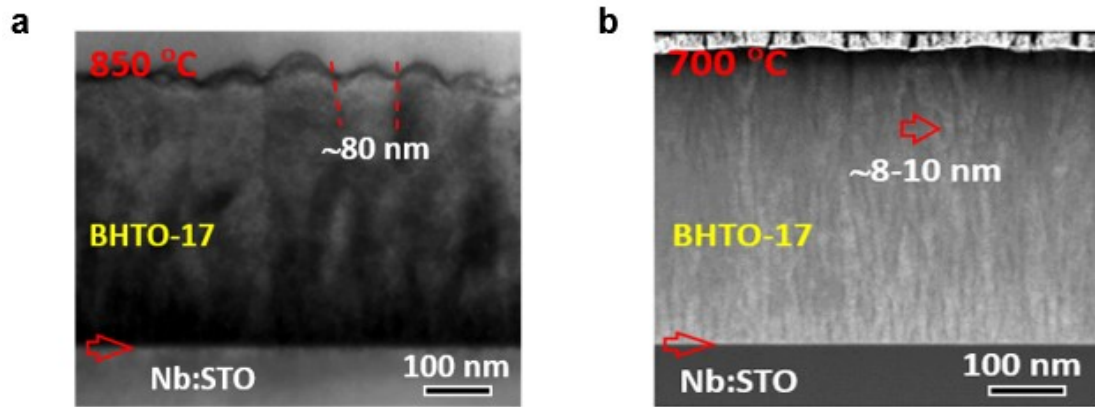
**Figure S7.** Electron micrographs showing the grain size of BHTO-17 films prepared at 850°C and 700°C. (a) A TEM image of the sample prepared at 850°C.　(b) A STEM image of the sample prepared at 700°C.

As we known, the growth temperature affects the growth rate and crystal nucleation, and directly determines microstructure of the films. The growth rate increases while nucleate rate decreases with the increase of the growth temperature. The relatively high growth rate and high diffusion rate at 850°C favor the formation of large-size grain, around 80 nm, as shown in Figure S7a. As the growth temperature decreases, the nucleation rate increases, but the diffusion rate decreases, which lead to the formation of nano-grains, around 8~10 nm at 700°C (Figure S7b). Thus, it can be concluded that as the growth temperature decrease, the homogeneous interfaces (or grain boundaries) increase and divide the large-size grains into nano-grains. These nano-grains show slight misorientation, leading to change of polarization at grain boundaries, behaving as nano-doamins, as shown in the simulation of local polarization behavior (Figure 1b). The polarization in a large domain in pure matrix is aligned along one direction, but the introduction of interfaces makes the polarization direction become random, and the area of polarization with the same direction becomes small in the nano-scale. This phenomenon is confirmed by the increased relaxor factor, which

represents the relaxor feature of the dielectric materials, as the homogeneous and heterogeneous interfaces increase (Figure S8). The value of relaxor factor is between 1 (normal ferroelectric with relatively large domain) and 2 (ideal relaxor ferroelectrics with nano-polar region). The relaxor factor of the structure of HOI@HEI@II is around 2, indicating that it is composed of nano-domains.
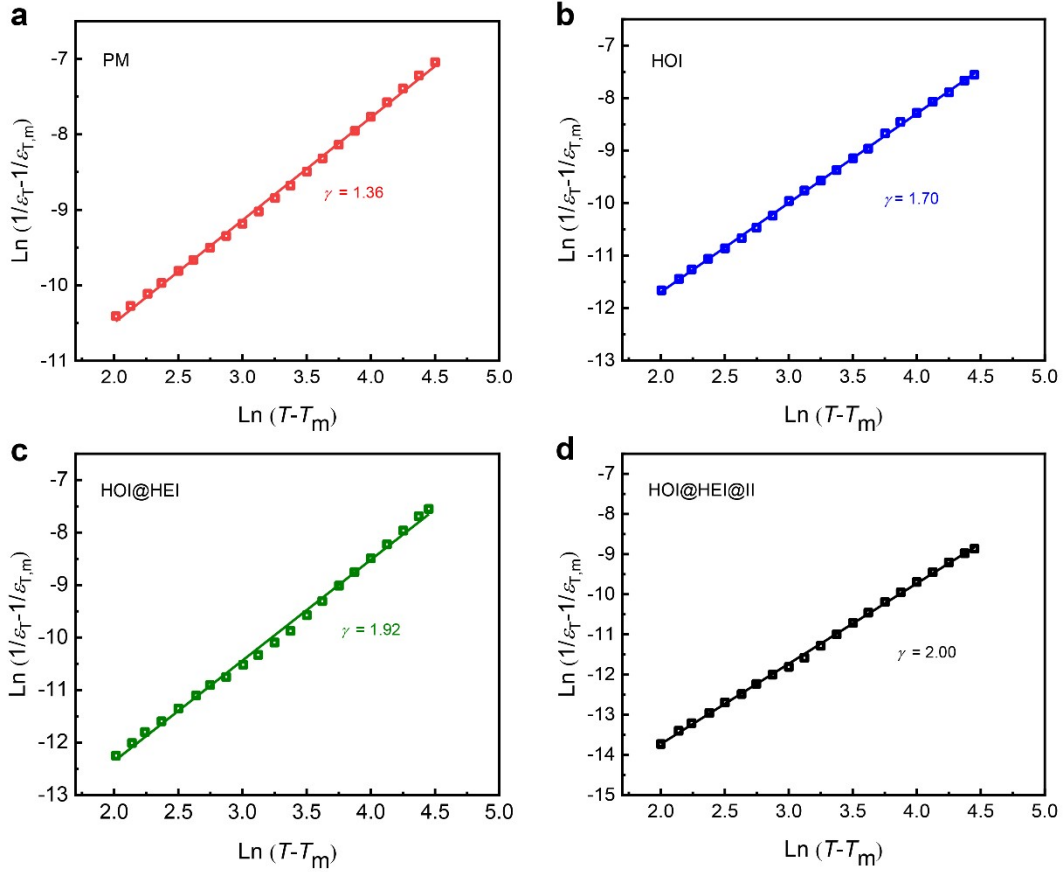
**Figure S8.** Fittings of the relaxor factor $\gamma$ of BHTO films with the modified Curie-Weiss law. Plots of $\ln(1/\varepsilon_T - 1/\varepsilon_{T,m})$ versus $\ln(T-T_m)$ of BHTO films at the frequency of 1 MHz. The relaxor feature of the RFE films can be quantitatively described by the relaxor factor ($\gamma$), which value between 1 (normal ferroelectrics) to 2 (ideal relaxor ferroelectrics).[3] The value of $\gamma$ increases gradually from 1.36 to 2.00 with increasing the interface. The factor $\gamma$ can be derived from the modified Curie-Weiss law

$$\frac{1}{\varepsilon_r} - \frac{1}{\varepsilon_{r,m}} = \frac{(T-T_m)^\gamma}{C} \tag{S17}$$

Where $\varepsilon_r$ is the permittivity at the temperature $T$; $T_m$ is the temperature at which $\varepsilon_r$ reaches the maximum $\varepsilon_{r,m}$. $C$ is a constant.
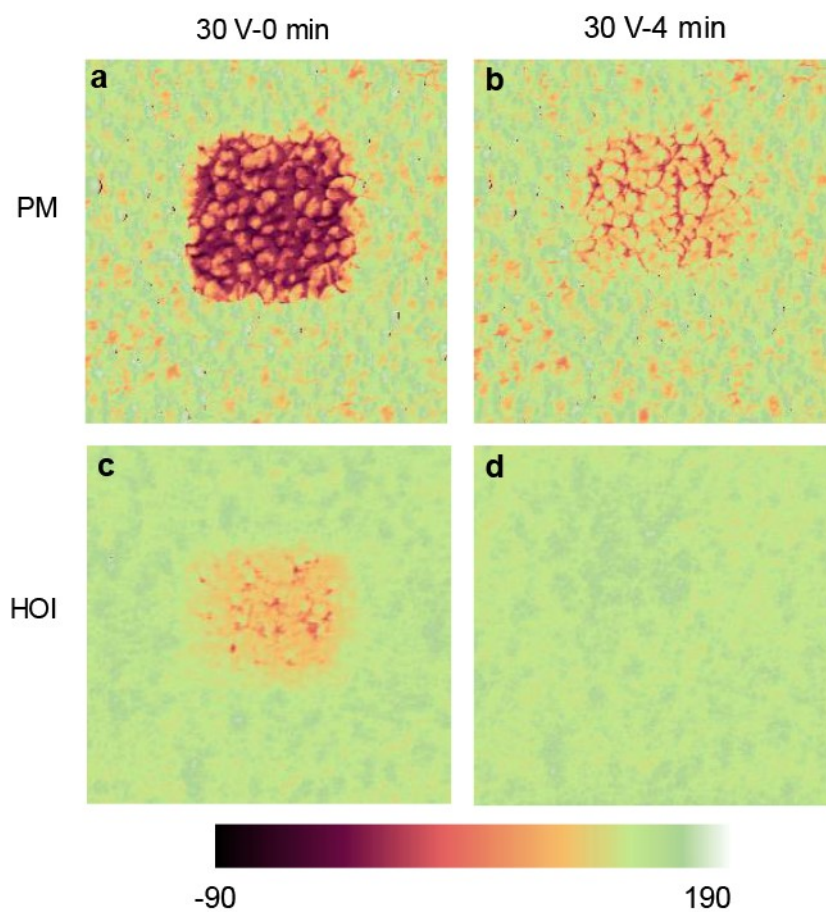
**Figure S9.** Poling behaviors of the BHTO films. Out-of-plane PFM amplitude images after poling treatment at 30 V with relaxation durations of 0 min and 4 min. (a) and (b) for PM, (c) and (d) for HOI.
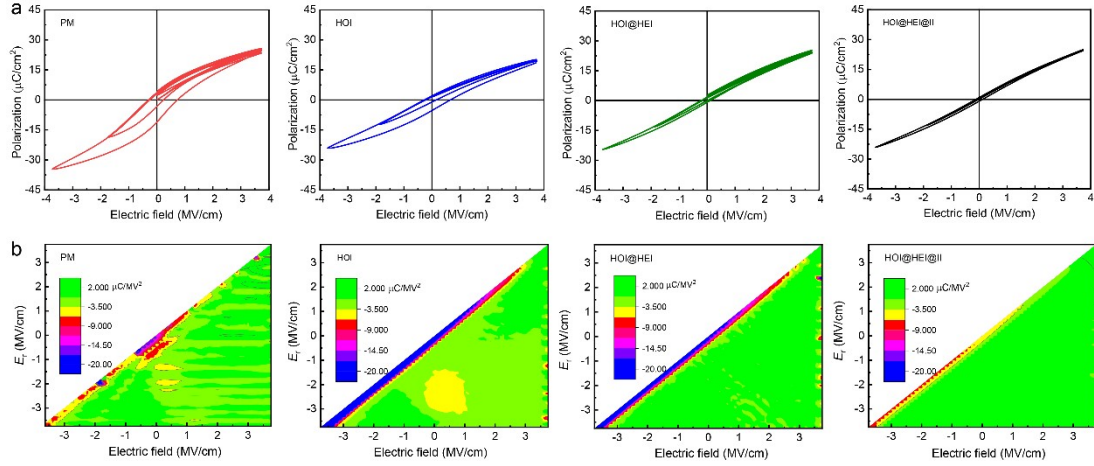
**Figure S10.** The first-order reversal curve loops (FORC) loops and corresponding evolution distribution of the BHTO films. (a) FORC loops of the BHTO films (only four out of the total 60 loops are shown for clarity). (b) Corresponding FORC distribution $\rho(E_r,E)$ of the BHTO thin films. The diagram of the PM film exhibits a low-intensity distribution zone located near the origin point, which reveals the strongly nonlinear polarization .With increasing the interface, the $\rho(E_r,E)$ becomes more evenly distributed in the whole electric field range, indicating nano-domains in the film enhance polarization switching and the distribution of coercive field is more uniform and relatively small.
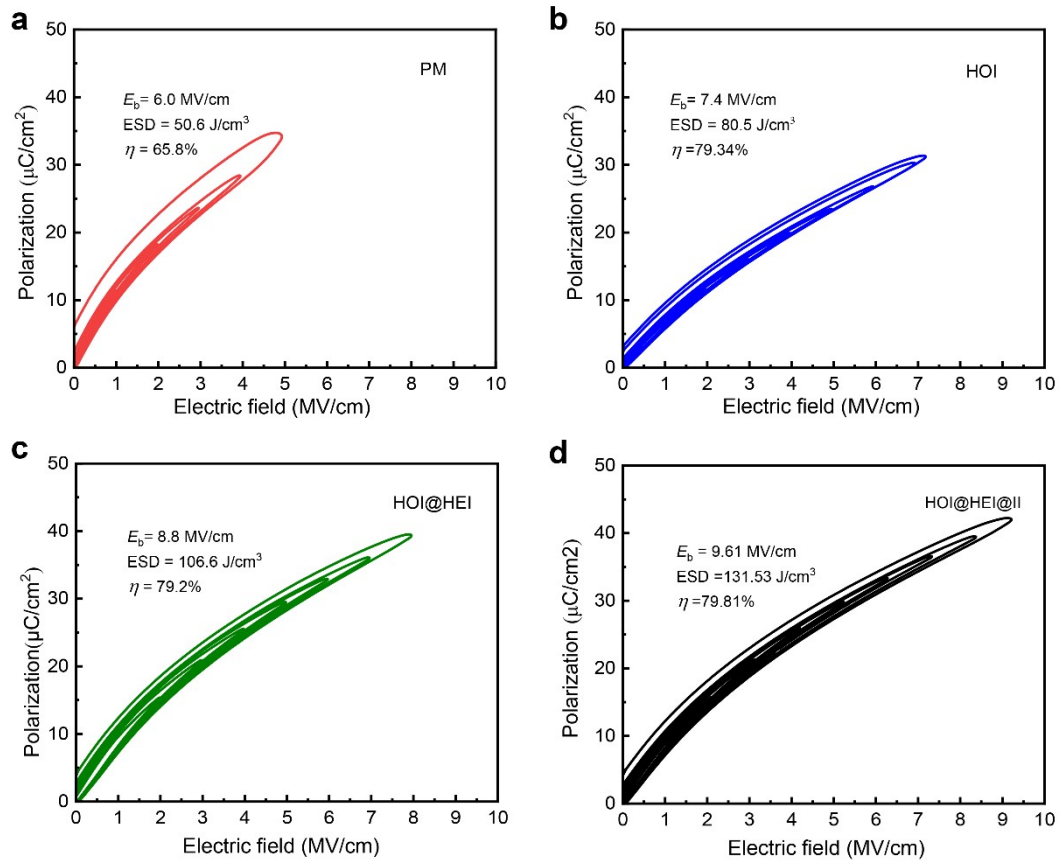
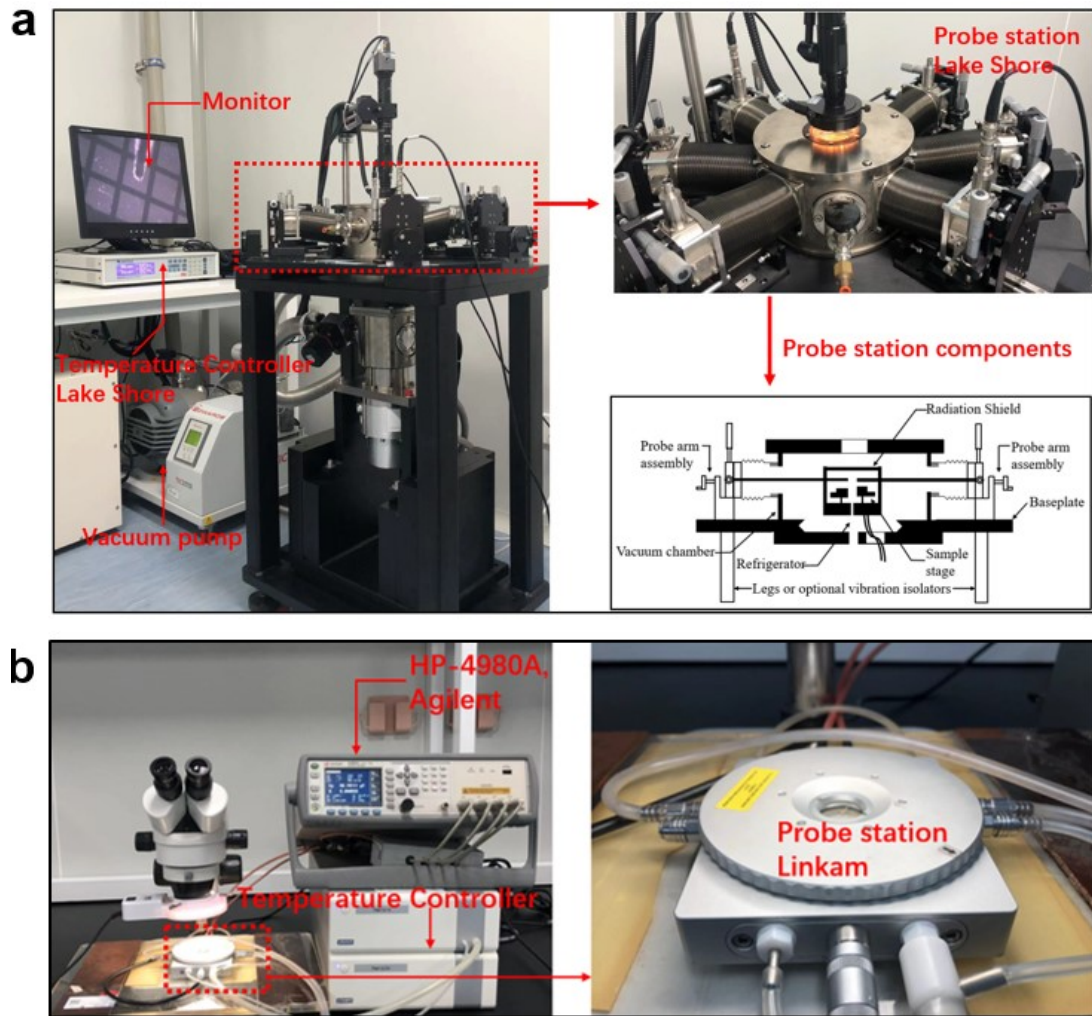**Figure S11.** Unipolar *P-E* loops of the BHTO films at 1 kHz. (a) PM, (b) HOI, (c)HOI@HEI and (d) HOI@HEI@II.

**Figure S12.** High temperature measuring Equipment. (a) Lakeshore cryocooled probe station and (b) Linkam temperature controller stage. Unipolar *P-E* loops, leakage current densities and power density of the BHTO films under vacuum conditions at different temperature (from -100 to 400°C) were accurately controlled by Lakeshore cryocooled probe station (CRX-6.5K, Lake Shore Cryotronics, Inc., USA). Dielectric permittivity and loss tangent of the films at different temperature (from 25 to 500°C) were provided through the Linkam stage (T95-PE, Linkam Scientic Instruments Ltd., UK).
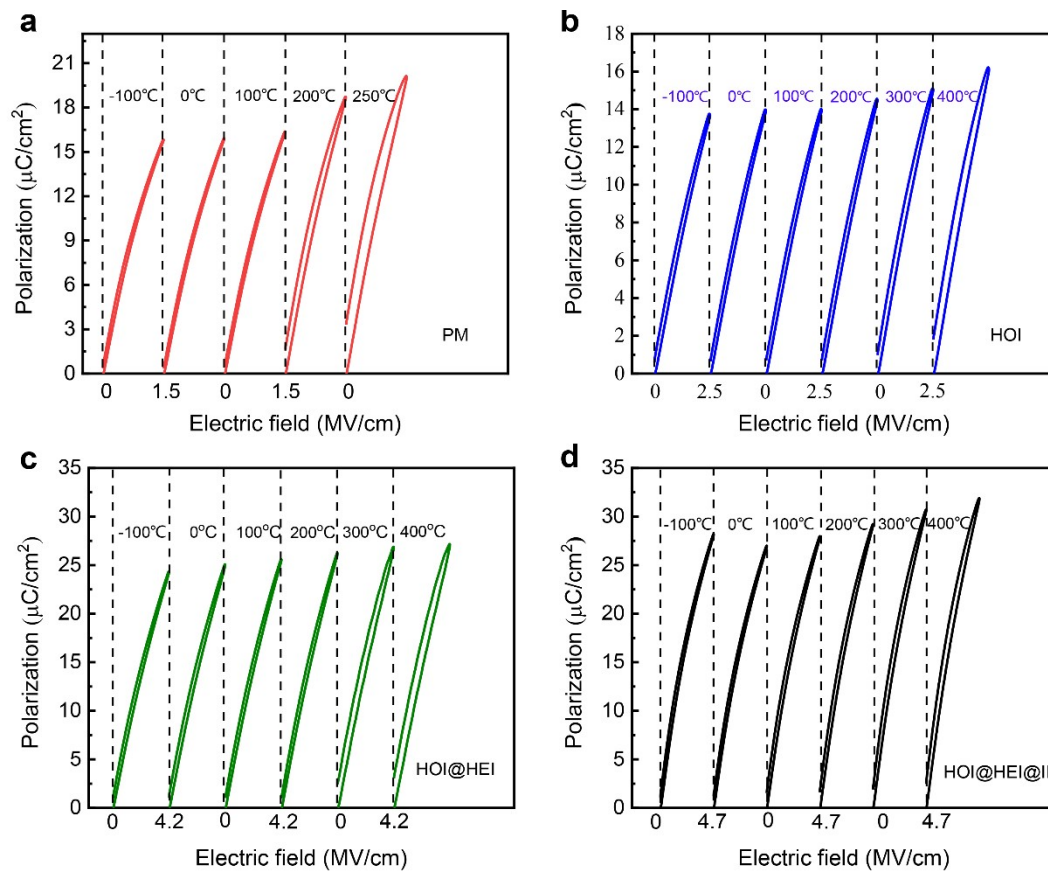
**Figure S13.** Unipolar *P-E* loops of the BHTO films measured at various temperatures under differrent electric field. (a) PM at 1.5 MV/cm, (b) HOI at 2.5MV/cm, (c) HOI@HEI at 4.2MV/cm, and (d) HOI@HEI@II at 4.7MV/cm.
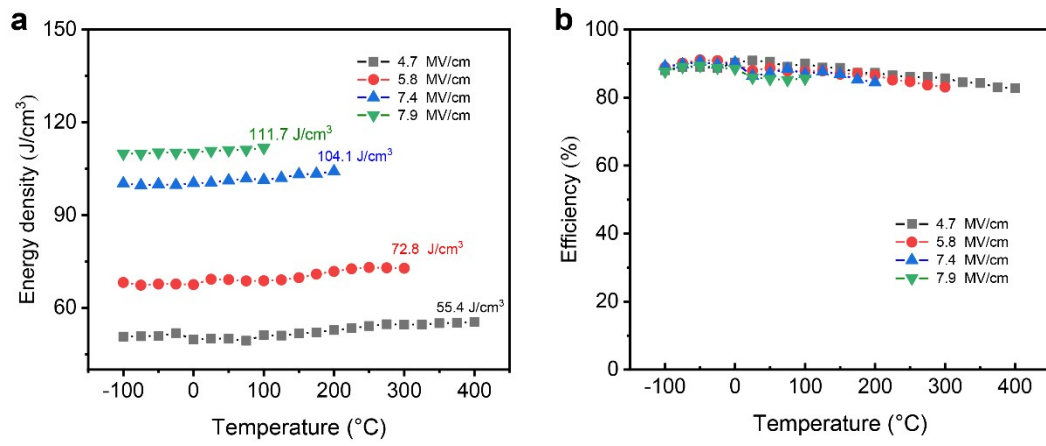
21

**Figure S14.** Temperature-dependent (a) energy density, and (b) efficiency of the HOI@HEI@II film at different electric fields.
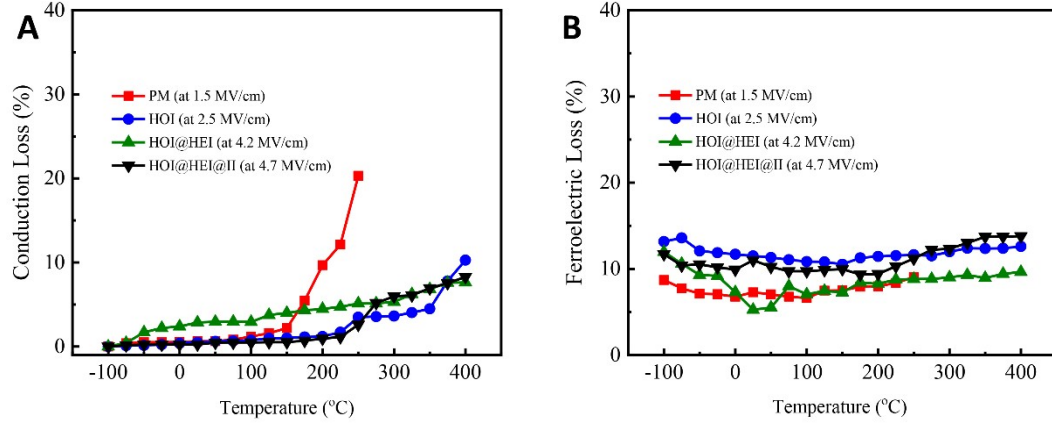
**Figure S15.** Temperature-dependent conduction and ferroelectric loss. (a) Conduction loss and (b) ferroelectric loss of the BHTO films measured at varied fields. Usually hysteresis loss consist of ferroelectric losses and conductivity losses. We assume that remnant polarization at -100°C comes entirely from ferroelectric losses.[9] After determining $\sigma_{eff}$ through equation (S25), the conductivity losses can be calculated via equation (S26)

$$P_{cond} = \frac{1}{2} \cdot \sigma_{eff} E^2 T \tag{S18}$$

$$U_{cond} = \frac{1}{3} \cdot \sigma_{eff} E^2 T \tag{S19}$$

where *T* is the period of the applied electric field. Dielectric losses may be calculated by subtracting conduction losses from total losses once $\sigma_{eff}$ has been determined. [9] The conduction loss and ferroelectric loss of he BHTO films at various electric fields are shown in Figure S15(a) and (b), respectively. The results reveal that at high temperatures, homogeneous and heterogeneous interfaces effectively suppress the conduction loss, lowering Joule heat generation and ensuring energy performance at high operating temperatures.
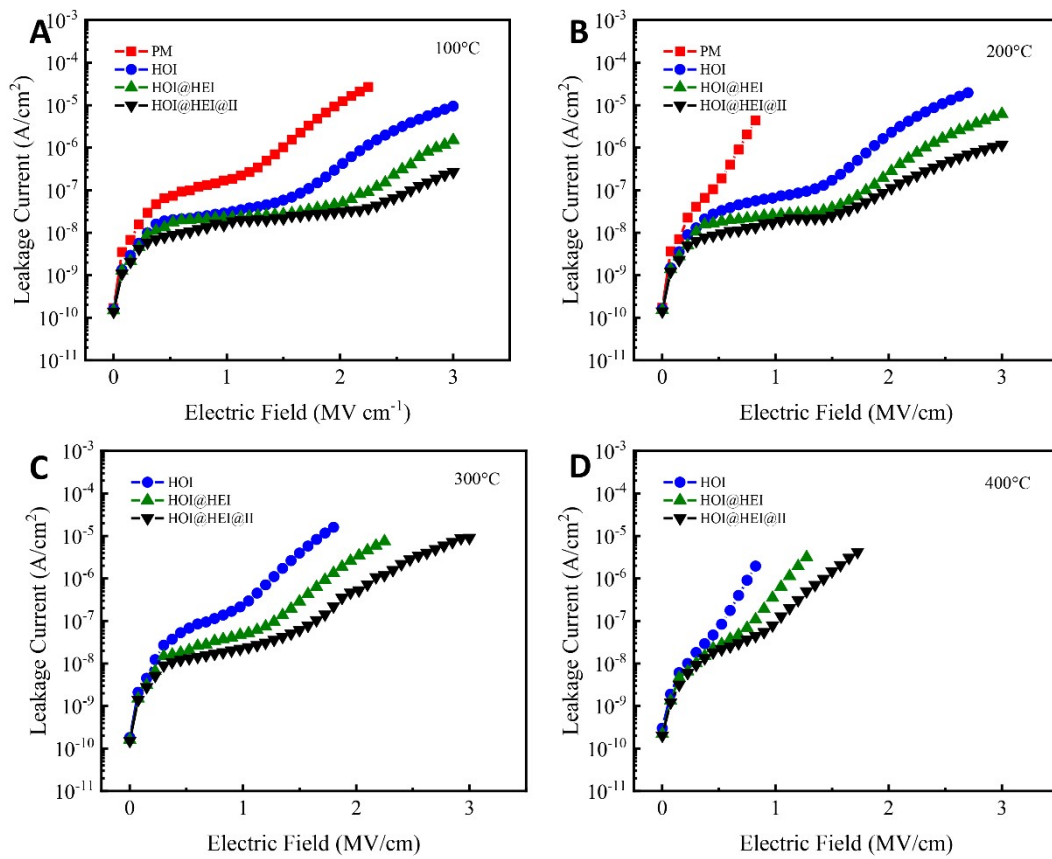
**Figure S16.** Leakage current densities of the BHTO films as a function of the biased electric field at various temperatures. (a) at 100 ºC, (b) at 200 ºC,(c) at 300 ºC, and (d) at 400 ºC.

**Supplementary Table S1.** Barrier heights $\phi_B$ (eV) of the interfaces between BHTO films and Pt at various temperatures.

|  | 25°C | 100°C | 200°C | 300°C |
|---|---|---|---|---|
| **PM** | 0.77 | 0.59 | 0.28 | - |
| **HOI** | 0.90 | 0.73 | 0.70 | 0.49 |
| **HOI@HEI** | 0.91 | 0.77 | 0.71 | 0.59 |
| **HOI@HEI@II** | 0.92 | 0.78 | 0.72 | 0.68 |

The barrier heights ($\phi_B$) at various temperatures are calculated from the slope of $\ln(J/E^2)$ vs ($E^{-1}$) in Figure S16.
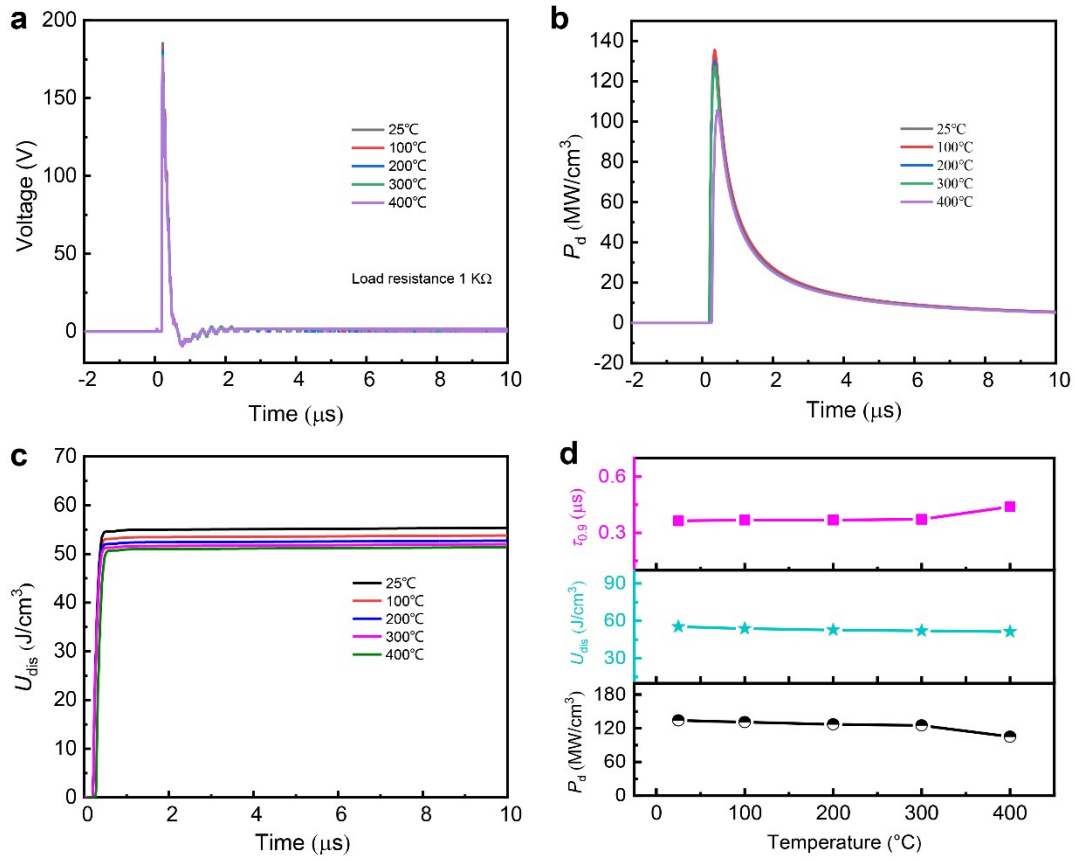
**Figure S17.** The energy discharge behaviors and power density performance of the HOI@HEI@II BHTO film at various temperatures. (a) Discharge voltage curve at different temperatures, (b) power density ($P_d$) at 4 MV/cm. (c) The discharged energy density ($U_{dis}$) at different temperatures. (d) The temperature stability of $P_d$, $U_{dis}$, and $\tau_{0.9}$ at different temperatures.

**References**

[1] S. B. Biner , S. Y. Hu, Acta. Mater. 57 (2009) 2088-2097.

[2] L. Niemeyer, L. Pietronero, H. J. Wiesmann, Phys. Rev. Lett. 52 (1984) 1033-1036.

[3] J. W. McPherson, K. Jinyoung, A. Shanware, H. Mogul, J. Rodriguez, IEEE. T. Electron. Dev. 50 (2003) 1771-1778.

[4] Z. Sun, C. Ma, M. Liu, J. Cui, L. Lu, J. Lu, X. Lou, L. Jin, H. Wang, C. L. Jia, Adv. Mater. 29 (2017).

[5] Q. Fan, M. Liu, C. Ma, L. Wang, S. Ren, L. Lu, X. Lou, C. -L. Jia, 51 (2018) 539-545.

[6] Q. Fan, C. Ma, C. Ma, R. Lu, S. Cheng, M. Liu, Appl. Phys. Lett. 116 (2020).

[7] H. Pan, F. Li, Y. Liu, Q. H. Zhang, M. Wang, S. Lan, Y. P. Zheng, J. Ma, L. Gu, Y. Shen, P. Yu, S. J. Zhang, L. Q. Chen, Y. H. Lin, C. W. Nan , Science 365 (2019) 578-582.

[8] L. Han, H. Ding, T. Huang, X. Wu, B. Chen, K. Ren, S. Fu, Plasmonics. 13 (2017) 1309-1314.

[9] H. Pan, J. Ma, J. Ma, Q. Zhang, X. Liu, B. Guan, L. Gu, X. Zhang, Y. J. Zhang, L. Li, Y. Shen, Y. H. Lin, C. W. Nan, Nat. Commun. 9 (2018) 1813.